




**Nanoscale surface roughness effect on Derjaguin-Landau-Verwey-Overbeek forces**

R. Bakhshandehseraji , G. Ch. Ponce de Leon , and G. Palasantzas   
*Department of Physics, Zernike Institute for Advanced Materials, University  
of Groningen, Nijenborgh 4, 9747 AG Groningen, The Netherlands*

F. Tajik

*Department of Condensed Matter Physics, Faculty of Physics, Alzahra University, Tehran 1993891167, Iran*



(Received 17 April 2024; revised 4 June 2024; accepted 10 June 2024; published 11 July 2024)

In this work we investigated the effects of nanoscale roughness on Derjaguin-Landau-Verwey-Overbeek (DLVO) forces using the proximity force approximation. To that end, the force between a gold-coated sphere and a plate, both immersed in pure and salt-added  $[\text{NaCl}] = 0.01M$  ethanol, was measured as a function of surface roughness with atomic force microscopy. The force data were compared with the predictions of DLVO theory with and without incorporating the contribution of surface roughness. It was observed that the surface roughness does not modify the qualitative behavior of the force-displacement curve but rather has a secondary influence by altering the values of the free parameters of the DLVO theory, namely, the Debye length and the electrostatic potential of the interacting bodies. In fact, it was found that the repulsive component of the force in pure ethanol increased with increasing roughness. These observations coincide with a positive correlation of the absolute value of the surface potentials with increasing surface roughness, suggesting that roughness effectively enhances the electric field near the surfaces, resulting in stronger electrostatic forces. For the salt-added solution, the contributions of the electrostatic forces are heavily suppressed, and the Casimir contribution plays the dominant role. Finally, we have shown that failure to incorporate the complete optical properties of the interacting metal bodies yields unphysical results for the free parameters of the electrostatic double-layer force.

DOI: [10.1103/PhysRevB.110.035416](https://doi.org/10.1103/PhysRevB.110.035416)

## I. INTRODUCTION

Surface forces are crucial in many technologically essential fields since they determine the behavior of systems such as, for example, colloids, cells, dispersions, micro- and nanofluids, and coatings [1]. Furthermore, in order to advance the development of micro- and nanoscale devices, it is essential to have fundamental knowledge of the ability to control the interfacial interactions at nanoscale separations in both air and aqueous media [1]. The DLVO theory, which was formulated by Derjaguin, Landau, Verwey, and Overbeek, has been the dominant description for interparticle forces for more than fifty years [2,3]. This formalism describes the forces between smooth surfaces in liquid as the sum of the van der Waals (vdW) and/or retarded van der Waals (Casimir) forces (as the dispersion force) and the electric double-layer (EDL) force (as the nondispersion force) [3,4].

The DLVO theory has been extensively investigated between different materials, e.g., mica sheets [5], silica, zinc sulfide [6,7], polystyrene [8], and alumina [9]. These studies, however, are especially challenging to perform due to the difficulty in finding proper surfaces for directly measuring the surface forces. For instance, for the data to be interpreted in a meaningful manner [2], the surfaces must be incredibly smooth and have the appropriate geometries for the chosen measurement technique. Moreover, force measurements between metallic and ceramic surfaces under electrochemical potential control [10–12] have revealed that the magnitude of

the forces at the molecular scale depends highly on the particular surface topography, and therefore they are affected by the roughness of the interacting surfaces. Indeed, surface roughness plays a pivotal role in these areas, which remarkably affect the physical and mechanical properties of surfaces [1]. Surface roughness is able to alter charge distribution; hence, the average plane of charges that generates the electrostatic double-layer interaction is shifted backwards with respect to the point of initial contact between the surface and an incoming probe as a result of the surface corrugation [13,14].

Consequently, dealing with rough surfaces makes the situation significantly more complicated, requiring further research and the development of more complex approaches. Therefore, in this study, we comprehensively investigated the influence of surface roughness on the DLVO theory using the proximity force approximation (PFA) to calculate forces as it is explained in Ref. [15]. To achieve this purpose, we compared the experimental force vs separation distance curves between a gold-coated sphere and plates of varying roughness, both immersed in pure and salt-added  $[\text{NaCl}] = 0.01M$  ethanol with the corresponding predictions of the DLVO theory with and without the incorporation of surface roughness, while maintaining a consistent ionic strength throughout our experiments unless explicitly mentioned otherwise. In what follows, we will refer to these two models, respectively, as the standard DLVO (S; without roughness) and the modified DLVO (R; with the incorporation of surface roughness).

## II. EXPERIMENTAL DETAILS AND SURFACE CHARACTERIZATION

In this study, we employed gold films grown by electron beam evaporation onto silicon wafers, which before deposition were rinsed as explained in Ref. [16]. Four different gold-coated substrate batches were made with varying thicknesses in the range of 100, 400, 800, and 1200 nm Au. For the first three substrates, we used an Au deposition rate of 0.1 nm/s, while for the rest of the substrates (thickest films) the deposition rate was increased to 1 nm/s in order to obtain rougher surfaces. Additionally, a borosilicate glass sphere (with a radius  $R \sim 10 \mu\text{m}$ ) was glued on cantilevers with spring constant  $k = 0.22 \pm 0.02 \text{ N/m}$ . The latter was obtained by hydrodynamic calibration within the fluid environment as it was explained in detail in our previous work [17]. Subsequently, the cantilever-sphere system was coated with 100 nm gold coating as it was explained in Ref. [17]. Prior to the deposition of Au from a 99.999% pure Au target at the pressure of  $10^{-6}$  bar, a 5-nm titanium (Ti) adhesion layer was deposited to improve the adhesion between the Au films and the silicon (Si) substrates in order to prevent delamination of the films during force measurements in aqueous environment. The fluid cells were rinsed with ethanol and deionized (DI) water and gently dried using  $\text{N}_2$ , and the Au surfaces were exposed to  $\text{N}_2$  airflow to avoid any possible contamination during force measurements.

Finally, all the force measurements were carried out using the Pico Force Multimode 8 atomic force microscope (AFM). The force curves were acquired in an ethanol solution, where in order to reduce the Debye length and minimize the repulsive double-layer force we also added salt,  $[\text{NaCl}] = 0.01M$ . Moreover, to minimize the impact of hydrodynamic drag force, the approach and retraction speeds were set at the minimum value of 50 nm/s. It must be noted that the hydrodynamic drag force  $F_{\text{hydro}} = -6\pi\eta R^2 v/h$  contribution (ignoring any slip effects) was subtracted from the total experimentally measured force. Here,  $h$  is the sphere-plate separation distance,  $R$  is the sphere radius,  $\eta$  is the medium viscosity, and  $v = 50 \text{ nm/s}$  is the relative velocity between the sphere and the plate surfaces [17,18].

Moreover, to measure accurately the probability density function  $f(z)$  and the distance upon contact,  $d_0$ , between the sphere and the plate, we performed a high-resolution scan in tapping mode as explained in Ref. [19] with the sharp tip. Eight topography images with a scan area of  $1 \times 1 \mu\text{m}$  and  $512 \times 512$  pixels were acquired at various surface positions of each plate, and the cumulative distribution function (CDF) of each image was computed (see the insets in Fig. 3, top right corner). The topography profiles of the gold-coated plate surfaces and spheres, which were used to investigate the roughness effect, were recorded using the Bruker Multimode 8 AFM operating in tapping mode. Furthermore, to characterize the front side of the sphere, where the interaction with the plate occurs, the inverse AFM in contact mode was used [17]. Finally, prior to combining eight images of each plate with the sphere image for the computation of the CDF of each thickness, the topography images were flattened to remove distortions due to the sample tilt and surface curvature (for the spheres) by subtracting first- and second-order degree

polynomials from each scan line of the images before any further processing.

## III. THEORETICAL MODELS: DISJOINING PRESSURE

In the following, we analyze the DLVO theory by studying the disjoining pressure,  $\Pi$ , between two plates separated by a distance  $h$ . The disjoining pressure is given by [20]

$$\Pi(h) = \Pi_e(h) + \Pi_C(h), \quad (1)$$

where  $\Pi_e(h)$  and  $\Pi_C(h)$  are the electrostatic and the Casimir disjoining pressures, respectively. For gold plates in ethanol, the Casimir contribution is always attractive, while the electrostatic contribution can be either attractive or repulsive depending on the sign of the potential at the surfaces.

### A. Casimir disjoining pressure for smooth surfaces

The Casimir contribution is obtained by means of the Lifshitz theory, which accounts for both the vdW force at short separations and the Casimir force at longer separations where retardation is important. The Casimir disjoining pressure is related to the Casimir energy  $E_C$  by differentiation ( $\Pi_C(h) = -dE_C/dh$ ). In turn, the Casimir energy  $E_C$  is given by

$$E_C(h) = k_B T \sum_{n'=0}^{\infty} \int \frac{d^2 k_{\parallel}}{(2\pi)^2} \ln(\det(\mathbb{I} - \mathbb{R}_1 \mathbb{R}_1 e^{-2k_{\perp} h})), \quad (2)$$

where the sum is carried over the Matsubara frequencies  $\xi_n = 2\pi k_B T n$ ,  $n \in \{0, 1, \dots\}$ . The apostrophe means that the term  $n = 0$  is multiplied by  $\frac{1}{2}$ , and  $k_{\perp} = (k_{\parallel}^2 + \varepsilon_{Et}(i\xi_n)\xi_n^2/c^2)^{1/2}$  with  $\varepsilon_{Et}(i\xi_n)$  denoting the permittivity of the dielectric medium between the two plates (assumed to be pure ethanol).  $c$  is the speed of light,  $\mathbb{I}$  is the  $2 \times 2$  identity matrix, and  $\mathbb{R}_1 = \mathbb{R}_1(i\xi_n, k_{\parallel})$  is the reflection matrix in the gap between the gold-coated plates. Both the reflection matrix and the permittivity must be evaluated at the imaginary angular frequency  $\omega = i\xi_n$  (see Supplemental Material Sec. A for the numerical implementation of Eq. (2) [21]).

Because the reflection matrix must be evaluated at imaginary frequencies  $i\xi_n$ , the permittivity of both the ethanol and gold must be analytically continued to the imaginary axis. Thus, it becomes necessary to consider frequencies that are beyond the available range of the experimental optical data. To bridge this gap, several alternatives are possible. One commonly used approach involves using the Drude model to describe the dielectric function of the metallic plates at low frequencies [22]. In the Drude model, the permittivity  $\varepsilon$  is given by

$$\varepsilon^{\text{Drude}}(\omega) = 1 - \frac{\omega_p^2}{\omega(\omega + i\omega_{\tau})}, \quad (3)$$

where  $\omega_p$  and  $\omega_{\tau}$  denote the plasma and relaxation frequency, respectively. The procedure follows by fitting the available optical data, obtained from ellipsometry measurements of the films, to extract the essential parameters from the Drude model, namely,  $(\omega_p, \omega_{\tau})$ . From the fitting we obtained (7.79 eV, 53.6 meV), (5.96 eV, 50.1 meV), and (6.74 eV, 50 meV) for the 100-, 800-, and 1200-nm Au films, respectively, as it is shown in Fig. 1. For the 400-nm Au film we used the

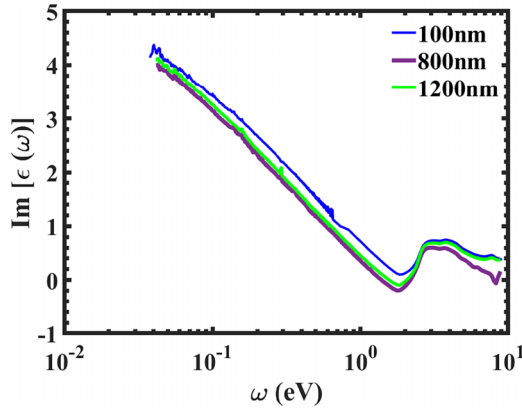


FIG. 1. Imaginary part of the dielectric function from the raw data of different thickness of gold surfaces.

plasma and relaxation frequencies as explained in Ref. [23]. Finally, to obtain the permittivity at the imaginary axis, Eq. (3)—describing a meromorphic function—can be evaluated at  $\omega = i\xi$ . Another approach involves setting  $\omega_\tau = 0$  in Eq. (3). This produces the so-called plasma model. Similarly to the Drude model, it can be analytically continued by simply evaluating the permittivity at  $\omega = i\xi$ . As a result we obtain

$$\varepsilon^{\text{plasma}}(i\xi) = 1 + \frac{\omega_p^2}{\xi^2}. \quad (4)$$

A more general approach relates the imaginary part of the permittivity at real frequencies,  $\varepsilon''(\omega)$ , to the permittivity at imaginary frequencies,  $\varepsilon(i\xi)$ , via a Kramers-Kronig-like relationship:

$$\varepsilon(i\xi) = 1 + \frac{2}{\pi} \int_0^\infty \frac{\omega \varepsilon''(\omega)}{\omega^2 + \xi^2} d\omega. \quad (5)$$

Nevertheless, the experimental values of  $\varepsilon''(\omega)$  are restricted to the range  $[\omega_{\min}:\omega_{\max}]$ , which means that the permittivity must be extrapolated for  $[0:\omega_{\min}]$  and  $[\omega_{\max}:\infty)$ . In the high-frequency range,  $\varepsilon''(\omega)$  is typically extrapolated using an inverse-third-power law (i.e.,  $\varepsilon''(\omega) \approx [\omega_{\max}^3 \varepsilon''(\omega_{\max})]/\omega^3$ , where the constant factors have been determined by continuity). Thus, the contributions of high frequencies to the integral in Eq. (5) can be expressed as follows:

$$\begin{aligned} \Delta_{\text{high}}(\xi) &= \frac{2}{\pi} \int_{\omega_{\max}}^\infty \frac{\omega \varepsilon''(\omega)}{\omega^2 + \xi^2} d\omega \\ &= \frac{2 \omega_{\max}^3 \varepsilon''(\omega_{\max})}{\pi \xi^2} \left[ \frac{1}{\omega_{\max}} - \frac{\frac{\pi}{2} - \arctan\left(\frac{\omega_{\max}}{\xi}\right)}{\xi} \right]. \end{aligned} \quad (6)$$

The contributions from the low frequencies to Eq. (5) can be accounted for by using the Drude model. In other words, the experimental data are fitted using Eq. (3) and those results are then extrapolated to perform the integration between  $[0:\omega_{\min}]$ , obtaining

$$\Delta_{\text{low}}(\xi) = \frac{2\omega_p^2\omega_\tau}{\pi} \int_0^{\omega_{\min}} \frac{d\omega}{(\omega^2 + \xi^2)(\omega^2 + \omega_\tau^2)}. \quad (7)$$

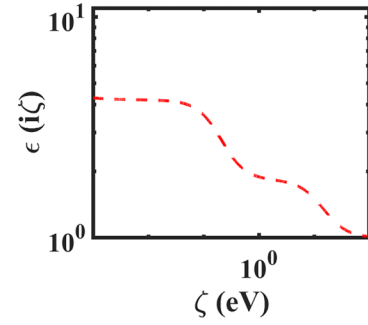


FIG. 2. Dielectric function at imaginary frequencies  $\varepsilon(i\xi)$  of ethanol as obtained by the three-oscillator model.

However, precision experiments performed in UHV and air between gold films [24,25] have shown that using the Drude model to extrapolate at low frequencies results in an underestimation of the Casimir contribution. The accuracy of the theoretical predictions can be improved by switching to the plasma model, where in essence one should set  $\omega_\tau = 0$  in Eq. (7). Combining the results of Eqs. (6) and (7) using the plasma model in Eq. (5) we obtain

$$\varepsilon^{\text{opt}}(i\xi) = 1 + \frac{\omega_p^2}{\xi^2} + \frac{2}{\pi} \int_{\omega_{\min}}^{\omega_{\max}} \frac{\omega \varepsilon''(\omega)}{\omega^2 + \xi^2} d\omega + \Delta_{\text{high}}(\xi), \quad (8)$$

which we refer to as the optical model. We remark that for similar values of  $\omega_p$  and for all values of  $\xi > 0$ ,  $\varepsilon^{\text{opt}}(i\xi) > \varepsilon^{\text{plasma}}(i\xi) > \varepsilon^{\text{Drude}}(i\xi)$ . One consequence of this inequality is that the optical model predicts the strongest Casimir force while the Drude model predicts the weakest [23,26]. The effect of these two descriptions on the estimation of the double-layer force is discussed in detail in Sec. IV B.

Finally, the dielectric function of ethanol at imaginary frequencies,  $\varepsilon_{\text{Et}}(i\xi)$ , as it is shown in Fig. 2, can be effectively formulated using the three-oscillator model as mentioned in Eq. (1) of Ref. [16]. It should be noted that this approach does not account for the influence of salt on the dielectric function.

### B. Electrostatic disjoining pressure for smooth plates

The electrostatic contribution  $\Pi_e(h)$  is obtained by solving the Poisson-Boltzmann equation. In the plane-plane geometry, the equation takes the form

$$\frac{d^2\Psi}{dx^2} = \frac{\rho(\Psi)}{\varepsilon}, \quad (9)$$

where  $\Psi(x)$  is the electrostatic potential at the distance  $x$ ,  $\rho(\Psi)$  is the charge density which is assumed to be a function of the potential only, and  $\varepsilon$  is the static permittivity of the solution in between the two surfaces (for ethanol  $\varepsilon = 25.07\varepsilon_0$  was used) [27]. For two metallic surfaces, a constant potential boundary condition is used. In other words, the electrostatic potential must satisfy the boundary conditions  $\Psi(0) = \Psi_1$  and  $\Psi(h) = \Psi_2$ . For both pure ethanol and with an electrolyte NaCl added in ethanol, the charge density is assumed to satisfy the condition [28]

$$\rho(\Psi) = -en_0 \left( e^{+\frac{e\Psi}{k_B T}} - e^{-\frac{e\Psi}{k_B T}} \right), \quad (10)$$

where  $e$  is the electron charge,  $n_0$  is the ion concentration,  $k_B$  is Boltzmann constant, and  $T$  is the absolute temperature (assumed to be 300 K). Derjaguin *et al.* [20] related the electrostatic potential  $\Psi$  to the disjoining pressure  $\Pi_e$  via the first integral of Eq. (9), yielding

$$\left(\frac{d\Psi}{dx}\right)^2 = \frac{2}{\varepsilon} \left[ en_0 k_B T \left( e^{\frac{e\Psi}{k_B T}} - 2 + e^{-\frac{e\Psi}{k_B T}} \right) - \Pi_e(h) \right]. \quad (11)$$

For the details on how to solve Eq. (11) to obtain  $\Pi_e(h)$  see Supplemental Material Sec. B [21]. It is worth noting that Eq. (11) is the complete nonlinear Poisson-Boltzmann equation; therefore, our calculations make no assumption about the magnitude of the electrostatic potentials at the metallic plates. Indeed, as will be shown later, the experimental values of these potentials often violate the condition  $e\Psi \ll k_B T$ , which makes any linearized approach unsuitable. Finally, in contrast with the Casimir term, the electrostatic contribution has free parameters not measured in the experiment, namely, the boundary potentials  $\Psi_1$  and  $\Psi_2$ , and the ion concentration  $n_0$ . This last term can be related to the Debye length,  $\lambda_D$ , via the following relationship:  $\lambda_D^2 = k_B T \varepsilon / 2e^2 n_0$ . Therefore, we will write  $\Pi_e(h; \Psi_1, \Psi_2, \lambda_D)$  for the electrostatic disjoining pressure of smooth surfaces.

### C. Proximity force approximation

With both the Casimir and electrostatic double-layer force contributions known, it is possible to relate the plate-plate disjoining pressure to the force between a sphere and a plate using the PFA. With the additional assumption of  $R \gg h$ , the sphere-plate force is given by

$$F_S(h; \Psi_1, \Psi_2, \lambda_D) = 2\pi R \int_h^\infty \Pi_S(u; \Psi_1, \Psi_2, \lambda_D) du, \quad (12)$$

which yields

$$F_S(h; \Psi_1, \Psi_2, \lambda_D) = 2\pi R E_c(h) + 2\pi R \int_h^\infty \Pi_e(u; \Psi_1, \Psi_2, \lambda_D) du \quad (13)$$

where  $\Pi_S(h; \Psi_1, \Psi_2, \lambda_D) = \Pi_e(h; \Psi_1, \Psi_2, \lambda_D) + \Pi_C(h)$  is the combined disjoining pressure, and Eq. (13) follows from  $\Pi_C(h) = -dE_c/dh$ . Here, the index S is added to indicate that Eq. (12) is the standard prediction of the DLVO theory without incorporating surface roughness effects.

### D. Roughness incorporation

When two rough bodies are brought into gentle contact, they are not in direct contact but are still separated by a certain average distance [29]. The absolute distance upon contact,  $d_0$  (the maximum peak within the effective area of interaction), is a pivotal factor [15]. The distance at which contact is established tends to be substantially greater than the RMS roughness measurement since it is determined by the presence of the most prominent surface asperities [30]. Therefore, if the contact area includes many asperities, the accurate contact occurs only in one or a few highest asperities [15]. Thus, a precise calculation is required to determine the highest peak

contribution to the force. To gain insight into the effects of roughness on DLVO theory, it is essential to address how the roughness modifies both the double-layer and the Casimir force. To provide clarity we employed a straightforward approach as explained in detail in Ref. [15] to calculate the roughness correction beyond perturbation theory. The method is based on the experimental fact that the distance  $d_0$  is significantly greater than the RMS roughness, as provided in Ref. [30]. According to Ref. [15] the interaction between two elastic rough surfaces (plates) can be viewed as the interaction between a rough inflexible plate and a smooth elastic plate [31,32].

Therefore, in this work we utilize Eq. (4) of Ref. [15] to investigate the roughness influence on the DLVO force. As it is stated in Refs. [15,22], if we know the probability density function (PDF)  $f(z)$  and  $d_0$  ( $d_0$  is the distance upon contact due to the highest asperities of both surfaces as shown in Fig. 3) then the disjoining pressure between the rough and flat surfaces is given by

$$\Pi_R(h; \Psi_1, \Psi_2, \lambda_D) = \int_{-d_0}^{d_0} f(z) \Pi_S(h-z; \Psi_1, \Psi_2, \lambda_D) dz \quad (14)$$

for  $h > d_0$ . Equation (14) is the convolution of the plate-plate disjoining pressure with the PDF of the combined height distribution  $f(z)$ . To obtain the force between a sphere and a plate with roughness incorporation  $F_R(h; \Psi_1, \Psi_2, \lambda_D)$ , it is enough to substitute  $\Pi_S$  by  $\Pi_R$  into Eq. (12). Thus, we obtain

$$F_R(h; \Psi_1, \Psi_2, \lambda_D) = 2\pi R \int_h^\infty \int_{-d_0}^{d_0} f(z) \Pi_S \times (u-z; \Psi_1, \Psi_2, \lambda_D) dz du, \quad (15)$$

$$F_R(h; \Psi_1, \Psi_2, \lambda_D) = \int_{-d_0}^{d_0} f(z) F_S(h-z; \Psi_1, \Psi_2, \lambda_D) dz, \quad (16)$$

where Eq. (16) follows by changing the order of integration. The function  $f(z)$  can be expressed as  $f(z) = dP(z)/dz$  with  $P(z)$  denoting the CDF, which can be extracted from the combined topography images by counting pixels with the height below  $z$  [19]. The combined profile of the two rough surfaces, as depicted in Fig. 15(b) in Ref. [15], measures the roughness in this configuration. Moreover, the parameter  $d_0$  represents the highest peak of the combined profile when the flat surface interacts with the rough surface [30].

### E. Maximum-likelihood models

To analyze the effects of roughness on the DLVO force, we will compare the same series of force-displacement curves using two models with and without roughness incorporation. These are summarized as  $Y_i = F_{S(R)}(X_i; \Psi_1, \Psi_2, \lambda_D) + \sigma Z_i$ . Here  $X_i$  is the experimental distance indexed by  $i$ ,  $Y_i$  is the experimental force at distance  $X_i$ , and  $F_{S(R)}(X)$  is the numerical solution of the DLVO force where the index S (R) indicates the model without (with) roughness. The experimental uncertainties are assumed to follow a Gaussian distribution with standard deviation  $\sigma$ .  $Z_i$  are independent and identically distributed random variables with  $Z_i \sim \text{Norm}(0, 1)$ . In the models described above,  $(\Psi_1, \Psi_2, \lambda_D)$  represent the

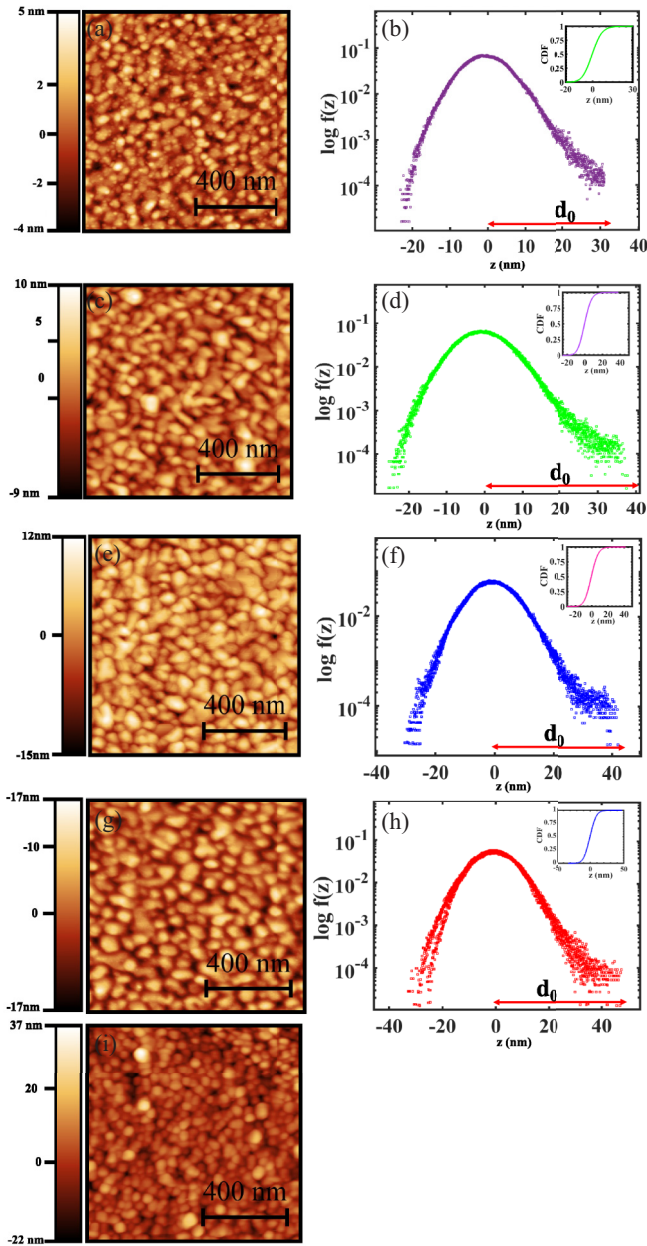


FIG. 3. Topography AFM scans of the rough surfaces, (a) 100 nm, (c) 400 nm, (e) 600 nm, and (g) 1200 nm in thickness of the Au films on Si with 1.2, 2.48, 3.9, and 4.91 nm RMS roughness, respectively. These are one out of eight AFM images that have been taken to consider the roughness incorporation. (i) 100-nm Au coated on borosilicate sphere which has been obtained by inverse AFM after removing the background curvature of the borosilicate sphere. [(b), (d), (f), (h)] Logarithm of the density function  $f(z) = dp(z)/dz$  of an area  $1 \times 1 \mu\text{m}^2$  from eight different AFM images at different locations on the surface of the Au films (100, 400, 600, and 1200 nm thickness, respectively), which were also combined with the AFM image of sphere. The corner top inset shows the cumulative distribution of the combined images, which is less than 1. (i) Inverse AFM topography of the 100-nm Au (with 6.3 nm RMS roughness) film on the borosilicate sphere after removing the special background curvature of the borosilicate sphere.

parameters of interest for the DLVO force, while  $\sigma$  is a nuisance parameter. The parameters ( $\Psi_1$ ,  $\Psi_2$ ,  $\lambda_D$ ,  $\sigma$ ) were determined from each experimental force-distance curve by maximizing the log-likelihood of the model. The confidence region for the fitting parameters was determined using the asymptotic form of the Wilks test (see Supplemental Material [21]). A converged partitioning method was used to numerically find the confidence region [33]. For the one-dimensional plot of the parameters, the confidence region was fit inside a three-dimensional (3D) box, and the extremes of the box were plotted. Therefore, all the uncertainties are systematically overestimated.

## IV. RESULTS AND DISCUSSION

In this section, we will discuss the results of the force measurements. We subdivide them into two sections (1) measurement in pure ethanol and (2) measurement with added salt,  $[\text{NaCl}] = 0.01M$  in ethanol. In all the analyses, only the force curves for surface separations between 50 and 300 nm were used unless stated otherwise.

### A. Pure ethanol

The force curves between a gold-coated sphere and plates with varying combined roughness in the unsalted solution are plotted in Figs. 4(a), 4(c), 4(e), and 4(g). These plots illustrate how an increasing surface roughness leads to an increase of the total force. The smoother sample [Fig. 4(a)], which has a combined RMS roughness of 8 nm, displays a total attractive force, while the rougher samples [Figs. 4(c), 4(e), and 4(g)] show a total repulsive force. Because the Casimir contribution is solely attractive for ethanol as the intervening medium, the main contribution to the force for the rough samples must arise from the repulsive EDL force. Moreover, this electrostatic contribution seems to diminish with diminishing roughness until it becomes comparable to or even smaller than the Casimir force for the smoothest sample. We must remark that the Casimir attraction becomes stronger for the rougher surfaces due to the contribution of the increasing high roughness peaks [15]. Nevertheless, the repulsive electrostatic force seems to be enhanced by surface roughness at a rate faster than the Casimir contribution, thus accounting for the increase in the total force with surface roughness.

Because the attractive Casimir contribution plays a secondary role in the unsalted solution, for the theoretical analysis we will model the permittivity of gold using the Drude model of Eq. (3). The results for the 68.27% confidence regions for the fitted parameters of the smoothest sample using both the standard and modified DLVO models are illustrated in Fig. 5. The maximum-likelihood parameters of both models describe in a satisfactory manner the experimental data (Fig. 4(a) and see Supplemental Material Sec. D for Tables 1, 2, and 3 [21]). What is more, the confidence regions of both models present significant overlap (see Fig. 5). Therefore, within our experimental sensitivity, the corrections due to 8-nm rms roughness to the DLVO model are statistically insignificant. Finally, we remark that the confidence regions

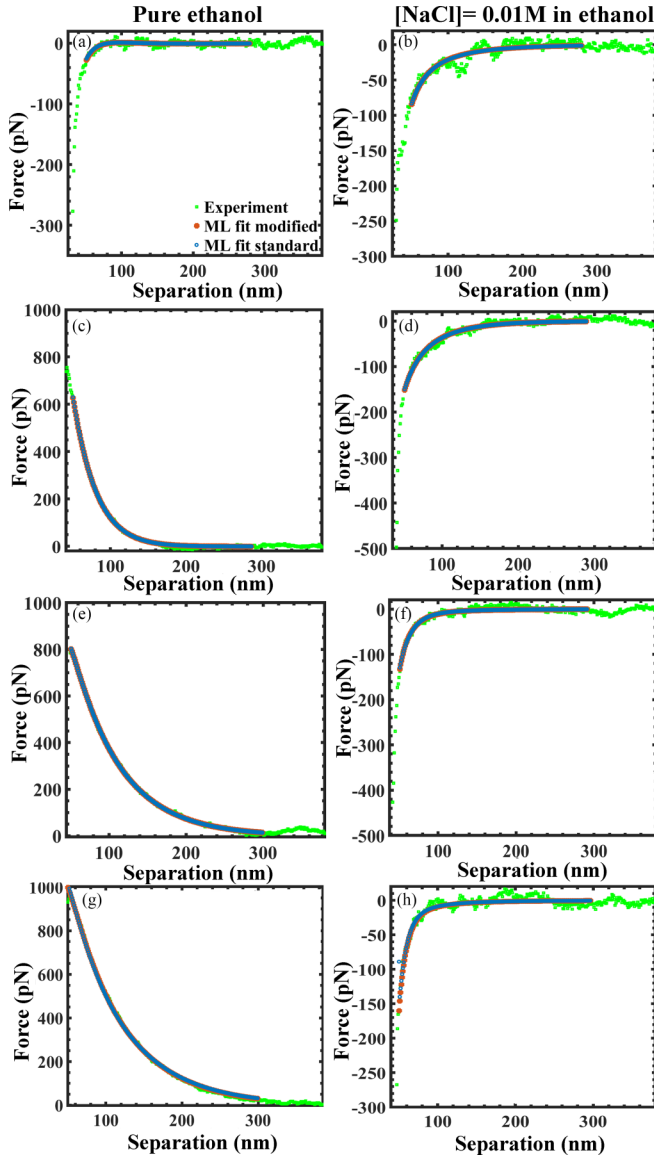


FIG. 4. Measured force vs separation distance for different surface roughness (where the sum of the roughness of the plate and the sphere ranges from 7.8 to 11.5 nm). Moreover, the plots represent a comparison between the two models, one incorporating roughness (modified) and the other without roughness (standard), within the framework of the DLVO theory. The force measurements took place in two different environments: pure ethanol, and added salt,  $[\text{NaCl}] = 0.01M$ , in ethanol. The force in (a) and (b) corresponds to an RMS value of 7.5, while the forces in (c) and (d), (e) and (f), and (g) and (h) are associated with RMS values of 9.0, 10.3, and 11.5 nm, respectively. The entire experimental data set is shown in green, while the outcomes for the modified and standard models are represented in orange and blue, respectively.

are skewed with respect to the axes defined by  $\Psi_1$ ,  $\Psi_2$ ,  $\lambda_D$ . This indicates that the effect of the parameters on the force is coupled. For instance, Fig. 5(d) illustrates that by decreasing  $\Psi_2$  while increasing  $\Psi_1$  an extremely similar force curve can be produced. This degree of correlation justifies *a posteriori* the need to perform a simultaneous three-dimensional parameter search.

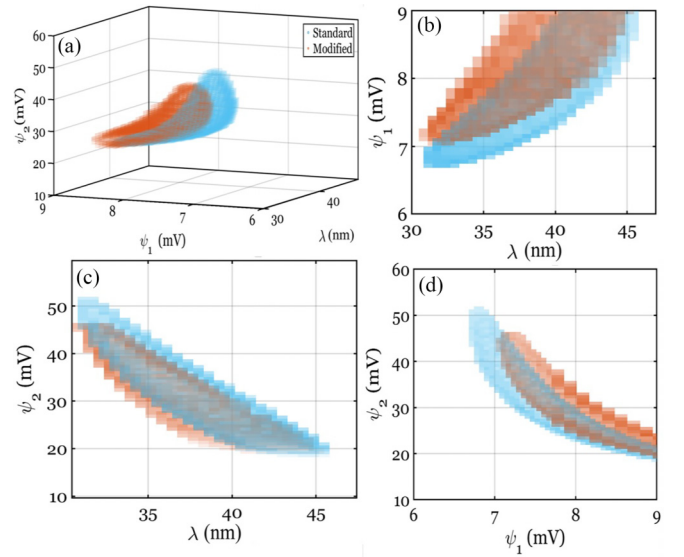


FIG. 5. (a) Three-dimensional confidence intervals for the smoothest sample (7.5 nm RMS) in pure ethanol. The 68.27% confidence region of the models with and without roughness present significant overlap. [(b)–(d)] Two-dimensional projections of the confidence interval. The oblong shape indicates that the parameters of the model (Debye length and surface potential) have a certain degree of correlation.

The samples with 9.0 and 10.3 nm RMS also present overlapping confidence regions. Only the sample with 11.5 nm rms exhibits a significant correction due to roughness. Its three-dimensional confidence region is illustrated in Fig. 6. It can be immediately seen that the confidence regions present no overlap in three dimensions. Moreover, the two-dimensional projections show that the region assigned to the modified DLVO model is smaller than for the standard DLVO model, implying an overall better fit (see Supplemental Material Sec. D for Tables 6 and 7 [21]). Unlike for the 8-nm sample, we were unable to obtain an upper bound for  $\Psi_2$ ; this, we argue,

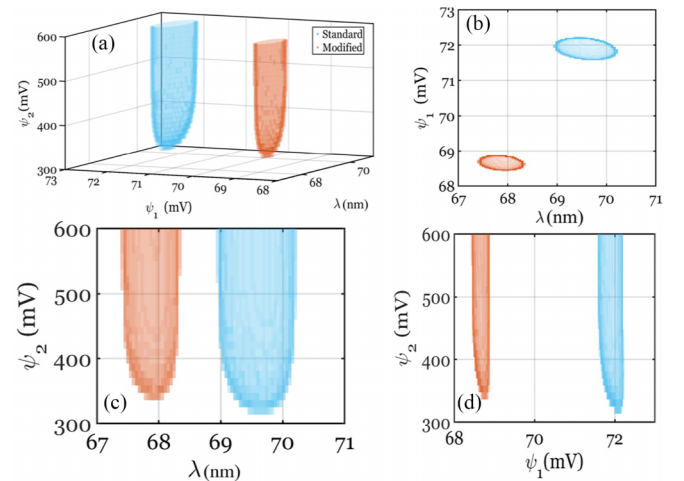


FIG. 6. (a) Three-dimensional confidence intervals for the most rough sample (11.4 nm RMS) in pure ethanol. The 68.27% confidence region of the models with and without roughness have no overlap. [(b)–(d)] Two-dimensional projections of the confidence interval. No upper boundary for the  $\Psi_2$  potential could be obtained.

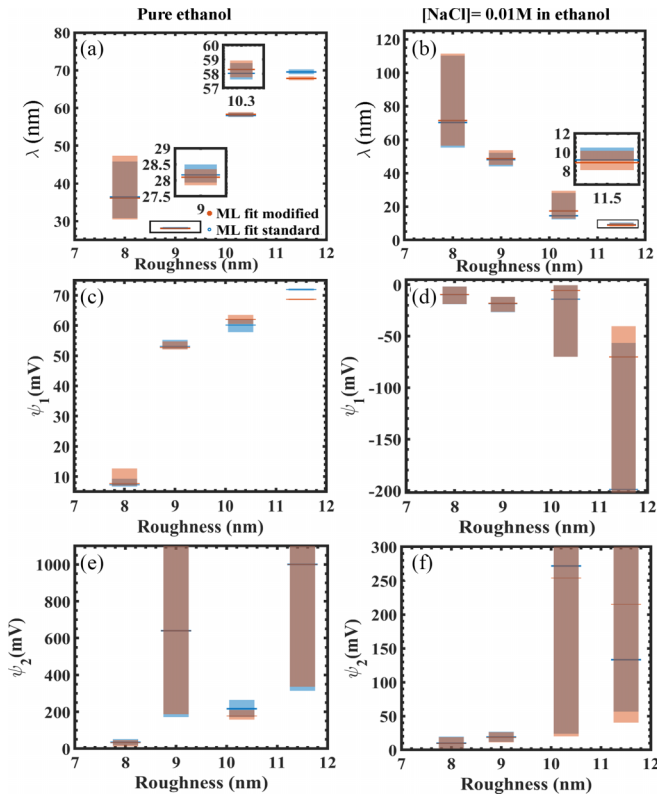


FIG. 7. Fit results of the standard and modified methods are depicted with confidence intervals. The maximum-likelihood estimates of the standard and modified methods are represented by blue and orange vertical lines, respectively. [(a) and (b)] Debye length vs roughness in pure ethanol and  $[\text{NaCl}] = 0.01M$  in ethanol. The inset represents our fitted results for RMS values of 9.0 and 10.3 nm to illustrate the predictions of two distinct models. [(c) and (d)] The surface potential  $\Psi_1$  between pure ethanol, and in  $[\text{NaCl}] = 0.01M$  in ethanol. The results account for the Casimir force using the Drude model only, which gives nonphysical results for the salted solution. [(e) and (f)] The surface potential  $\Psi_2$  between pure ethanol and  $[\text{NaCl}] = 0.01M$  in solution.

is a consequence of the exponential dependence of Eq. (10) with the surface potentials (see Supplemental Material Sec. C [21]). Therefore, ignoring the contributions of roughness results in an artificial increase in the Debye length and the surface potential  $\Psi_1$ . This comes as no surprise, since the contribution of the high roughness peaks augments the force [15]. Therefore, to account for this increase—in the absence of roughness—the potential  $\Psi_1$  and/or  $\lambda_D$  must rise since higher values of those parameters result in a stronger force.

The relationship between the fitted Debye length and the RMS roughness for the S and R models for pure ethanol is illustrated in Fig. 7(a), where we have presented the minimum and maximum values of the Debye length of the three-dimensional confidence region. For most of the samples, the incorporation of roughness into the DLVO theory had a small effect on the fitted Debye length. Nevertheless, our data seem to show a secondary trend: a positive correlation between the Debye length and surface roughness. However, we must be careful about establishing such a relationship, since the theoretical value for the Debye length  $\lambda_D$  of ethanol ( $\text{pK}_a \sim 15.4$ ) would be hundreds of nanometers, which is never observed.

The reason lies in the presence of impurities. Indeed, commercial chemically pure ethanol has been reported in the scientific literature to have a Debye length ranging from 20 to 100 nm [25]. Our fit results, as illustrated in Fig. 7(a), are compatible with these observations for  $\lambda_D$ . Although the equipment utilized during force measurements was thoroughly rinsed with ethanol and DI water three times and then dried before each measurement, our current experimental setup cannot definitively assert the relation between the Debye length and surface roughness. To that end, independent measurements of the salt concentration (for instance, by measuring electrical conductance) should be performed.

Figures 7(c) and 7(e) illustrate the relationship between the fitted values for the surface potentials  $\Psi_1$  and  $\Psi_2$ , and the corresponding RMS roughness of the samples. Notably, for the vast majority of samples, the absolute values of the potentials violate the equality  $e|\Psi| \ll k_B T$  ( $\approx 25$  meV at room temperature). This justifies the need to incorporate the full nonlinear form of Eq. (10). Our trade-off, as it was mentioned before, was the inability to fully bind the values of the potentials to 68.27% confidence using our fitting procedure. This issue arises from the nature of Eq. (10) because the dependence of the potentials is exponential. As a result, small increments of their values have little effect on the force-displacement curve for the separation distances studied in this work (see Supplemental Material Sec. C [21]). Therefore, for those occasions, only one bound could be obtained. These, however, give enough information to discern important trends. The smallest surface potential,  $\Psi_1$ , follows a straightforward monotonic increase with increasing roughness. The case for the maximum-likelihood values of  $\Psi_2$  becomes more complex; however, the lower bound still exhibits an increasing trend with roughness. It is unlikely that the true value of the surface potentials lies well above 500 mV, and thus the large values of the maximum likelihood might be a mathematical artifact due to our inability to obtain an upper bound. More likely, the true values of the higher potential  $\Psi_2$  may lie closer to the lower bound.

With that in mind, we put forward an explanation for the observed enhancement of the electrostatic double-layer force with surface roughness. We conjecture that, for a fixed value of the surface potential, the presence of rough asperities effectively produces a local increase of the electric field near the surface, thus resulting in stronger electrostatic interactions and a stronger repulsive force. Because standard DLVO theory assumes that the double-layer force arises from flat surfaces, the only way for the model to account for stronger electric fields is if the absolute value of the surface potentials increases. This is consistent with the trend observed in Figs. 7(c) and 7(e). The situation is no different for the modified DLVO theory since the PFA only accounts for the geometric variations in separation created by roughness—which are present in all rough samples—but does not include any changes to the electric field generated by the asperities.

Overall, incorporating roughness in DLVO using the PFA has little effect on the majority of samples, as can be seen by the overlapping confidence regions. The geometric effect of roughness only comes into play when the forces are considerably strong [Fig. 4(g)], due to a combination of strong potential and/or large values of the Debye length. Therefore,

roughness seems to play a secondary role by changing the free parameters of the model, ( $\Psi_1$ ,  $\Psi_2$ ,  $\lambda_D$ ), likely due to the enhancement of the electric field near the surface.

### B. [NaCl] = 0.01M in ethanol

The force-displacement curves for the salted solution of [NaCl] = 0.01M in ethanol are illustrated in Figs. 4(b), 4(d), 4(f), and 4(h). In this situation, the charge concentration is increased, leading to a smaller Debye length and as a result a significant reduction in the electrostatic double-layer force. Therefore, the Casimir force plays the dominant role, resulting in a total attractive force. We observed that the experimental force was significantly stronger than the Casimir force predicted by Lifshitz theory using the Drude model. This discrepancy can be modeled as a remnant attractive electrostatic force, which means that the surface potentials now have opposite signs. We remark that Eq. (10) fixes the zero of the potential as the voltage at which the solution has no charge density. The presence of salts is likely to change this zero of the potential as compared with the pure ethanol case, accounting for the switch in signs.

The fitted results with their confidence intervals are illustrated in Figs. 7(b), 7(d), and 7(f). For all samples, the confidence intervals overlap, suggesting no significant geometrical effects due to roughness. This is expected since the double-layer force is considerably smaller, and we only observed significant geometrical effects for the strongest force in the previous section. Furthermore, in this scenario, the highest Debye length is observed on the smoothest surface, and subsequently, the Debye length experiences a gradual decrease with an increase in roughness as shown in Fig. 6(b). However, the fitted values of the Debye length are unphysical, especially for the smoothest samples, which yield a value higher than that in pure ethanol. Indeed, at a concentration of [NaCl] = 0.01M, the theoretical value of the Debye length is  $\sim 3$  nm. This unexpected trend suggests that the estimation of the Casimir force using the Drude model is inadequate for this scenario. Indeed, as was mentioned in Sec. III A, the Drude model underestimates the Casimir contribution, thus resulting in a fictitious increase of the electrostatic double-layer force. Therefore, to improve the accuracy of the fits when the Casimir contribution is dominant, we switched to the optical model, which accounts for the optical properties of the gold film.

### C. [NaCl] = 0.01M in ethanol with the optical model

The results after implementing the optical model are illustrated in Figs. 8(a), 8(c), 8(g), and 8(e). The fitted parameters and their confidence interval for the Debye length are illustrated in Fig. 8(d); as expected, there is a notable reduction in the Debye length value. Moreover, in contrast to the pure ethanol case, the Debye length seems to diminish with increasing roughness. This is consistent with the possibility that surface roughness augments the accumulation of charges near the surfaces, resulting in a smaller Debye length. Nevertheless, as mentioned previously, within our current experimental setup we cannot rule out the contribution of impurities in the observed trend.

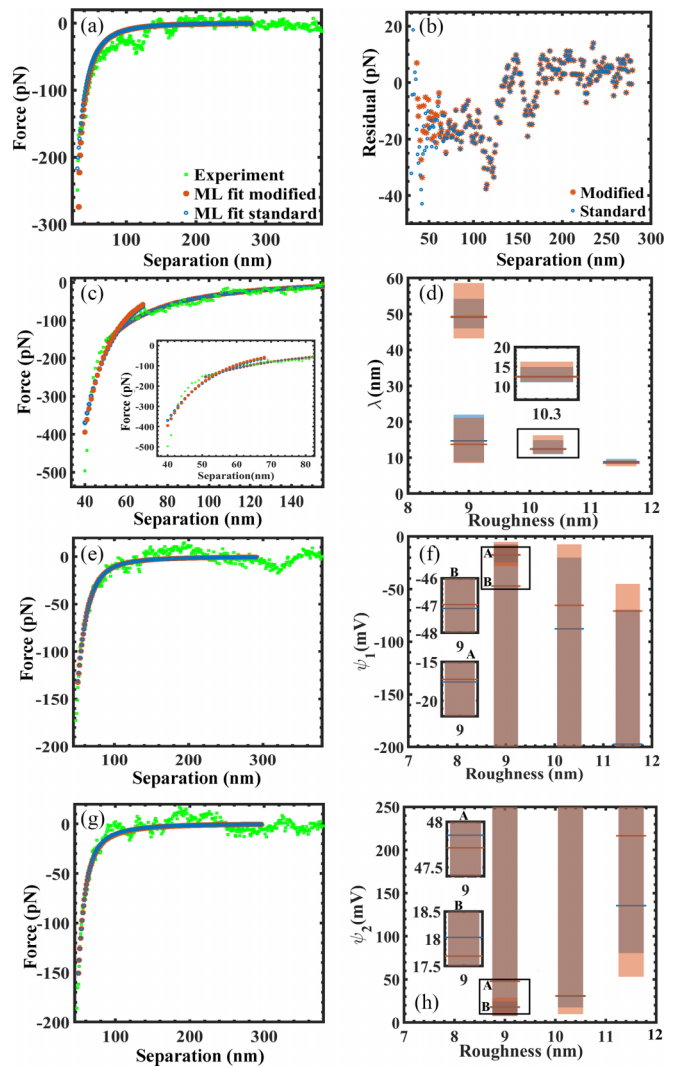


FIG. 8. Fit results of the standard and modified methods are depicted with confidence intervals in [NaCl] = 0.01M in ethanol using the optical model. [(a), (c), (e), (g)] The measured force roughness and the corresponding  $t$  curves obtained by the optical model. The inset of (c) indicates the  $t$  for small separation distances (30–70 nm). [(b)] The residual of the smoothest surface (RMS 7.8 nm). [(d), (f), (h)] The Debye length and surface potential ( $\Psi_1$  and  $\Psi_2$ ) vs surface roughness. The insets labeled A and B illustrate  $t$  results at small and large separation distances, respectively. The maximum-likelihood estimates of the standard and modified methods are represented by blue and orange dashes.

Quite surprisingly, by employing the optical model, we did not observe any remnant electrostatic contribution for the smoothest film. Indeed, the residue between the experimental force and the predictions of the Casimir force using the optical model is shown in Fig. 8(b). As can be seen, the remaining signal is within the noise level of our experiment. Thus, for the smoothest film, the electrical double-layer force lacks sufficient strength to be observed experimentally. This has important implications for Casimir-related experiments in liquids which may benefit by suppressing nongenuine contributions to the Casimir force—like the



electrostatic double-layer force—by improving the smoothness of the surfaces.

In the case of the 9-nm RMS surfaces, we encountered the necessity of conducting fitting within two distinct ranges. Since the Debye length did not demonstrate the expected reduction within the range 50–300 nm, we considered possible causes. We believed that the noise contribution in the distance range between 50 and 300 nm might be stronger than the contribution of the remnant electrical double-layer force. This issue can be solved by performing the fit over shorter separation distances (30–70 nm), where the signal-to-noise ratio is the largest. The results of this second fit are shown in the inset of Fig. 8(c). As can be seen, the fit at shorter distances predicts a smaller (and more reasonable) value of the Debye length as compared with the fit at large separation distances. Their respective fitted values are illustrated in Fig. 8(d) with labels A and B for the short- and long-distance range, respectively.

Regarding the surface potential, both the optical model and the Drude model provide comparable descriptions of the behavior of the surface potential. As shown in Figs. 7(c) and 7(e) and Figs. 8(f) and 8(h), the surface potentials  $\Psi_1$  and  $\Psi_2$  exhibit a steady upward trend as the surface roughness increases, displaying negative and positive values of the surface potentials, respectively. This observation is consistent with the explanation put forward in the previous section; in essence, the surface asperities locally enhance the electric field, resulting in an effective increase in the absolute value of the potentials with roughness.

Comprehensive information on the Debye length, and surface potentials with lower and upper boundary in the pure ethanol and in the salted solution, can be obtained by the fit results provided (see Supplemental Material Sec. D for Tables 1–5 [21]). Additionally, in order to elucidate the deviation between the experimental results and the S and R model predictions for both the Drude and plasma models,  $\sigma$  and  $R^2$  values have been included (see Supplemental Material Sec. D for Tables 5 and 6 [21]).

## V. CONCLUSIONS

In summary, we have investigated the pivotal influence of nanoscale roughness on the DLVO theory between surfaces upon contact in a pure ethanol environment, and with salt  $[\text{NaCl}] = 0.01M$  added in ethanol solution. The fitting parameters of the standard DLVO (S) and roughness DLVO (R) models yield similar results for most values of the combined RMS roughness of the interacting surfaces as is evidenced in the overlapping 68.27% confidence regions. The latter demonstrates that surface roughness does not modify the qualitative behavior of the force-displacement curve. The roughness, however, is significantly correlated with the parameters of the model. Indeed, we observed that the Debye length follows a monotonic increase with increasing roughness in the pure ethanol ambient, whereas after salt is introduced, the Debye length decreases with increasing surface roughness. This trend, however, cannot be definitively established with

our current experimental setup, due to our inability to account for the effects of contaminants in the trend. For future experiments, independent measurements of the Debye length should be performed, for instance, by measuring the electric conductivity with a three-terminal method.

In both models (standard DLVO and roughness DLVO models), whether in pure ethanol or  $[\text{NaCl}] = 0.01M$  in ethanol, the absolute value of the surface potentials  $\Psi_1$  and  $\Psi_2$  tends to increase with increasing roughness. We propose a microscopic explanation for this observation in terms of local electric field enhancement due to the roughness asperities. The DLVO theory with the PFA can only incorporate the geometric effects of roughness but does not account for modifications of the electric field near the surface. This offers an interesting problem for theoretical investigation. Indeed, a model that incorporates roughness at the level of the Poisson equation might yield more adequate results. Moreover, the fitted values of the surface potentials, most of them above 25 mV, illustrate the need to incorporate the full nonlinear form of the Poisson-Boltzmann equation. Undeniably, this came with the inability to fully bind the value of the surface potentials. Therefore, future efforts could also focus on improving the numerical techniques presented in this work to obtain a complete bound for the confidence interval.

Finally, we have shown how failing to account for the optical properties of the films yields unphysical values for the Debye length in  $[\text{NaCl}] = 0.01M$  in ethanol. This illustrates the importance of fully characterizing the films for experiments aiming to study dispersion forces. What is more, we showed that using smooth films can meaningfully suppress the electrostatic contribution in the salted solution, which is of great relevance for Casimir-related experiments. It is worth mentioning that our calculations using the Lifshitz theory completely ignored the contributions of the salt to the Casimir force. Recent theoretical investigations have revealed that in salted solutions, an additional longitudinal electromagnetic mode is present due to movable ions [34]. While this mode modifies the Casimir force, we estimated its contribution to be smaller than 1 pN for our experimental setup, which is within the noise level and it can be safely discarded. The effect of the ions on the dielectric permittivity of ethanol raises another important point, to our knowledge, no universally accepted approach has been developed so far, thus presenting an interesting topic for future studies. This creates a compelling avenue for future research endeavors in the field of electrochemistry and materials science.

The data that support the findings of this study are available from the corresponding author upon reasonable request.

## ACKNOWLEDGMENTS

We would like to thank Gert ten Brink and Hans de Vries for the technical support, as well as P. A. Maia Neto and V. B. Svetovoy for useful discussions. This research was supported by the Netherlands Organization for Scientific Research (NWO) under Grant No. OCENW.KLEIN.179.

- [1] M. Valtiner, K. Kristiansen, G. W. Greene, and J. N. Israelachvili, Effect of surface roughness and electrostatic surface potentials on forces between dissimilar surfaces in aqueous solution, *Adv. Mater.* **23**, 2294 (2011).
- [2] N. Eom, D. F. Parsons, and V. S. J. Craig, Roughness in surface force measurements: Extension of DLVO theory to describe the forces between Hafnia surfaces, *J. Phys. Chem. B* **121**, 6442 (2017).
- [3] B. W. Ninham and P. L. Nostro, *Molecular Forces and Self Assembly: In Colloid, Nano Sciences and Biology* (Cambridge University Press, Cambridge, UK, 2010).
- [4] V. Agmo Hernández, An overview of surface forces and the DLVO theory, *ChemTexts* **9**, 10 (2023).
- [5] S. Biggs and P. Mulvaney, Measurement of the forces between gold surfaces in water by atomic force microscopy, *J. Chem. Phys.* **100**, 8501 (1994).
- [6] G. Toikka, R. A. Hayes, and J. Ralston, Surface forces between spherical ZnS particles in aqueous electrolyte, *Langmuir* **12**, 3783 (1996).
- [7] T. H. Muster, G. Toikka, R. A. Hayes, C. A. Prestidge, and J. Ralston, Interactions between zinc sulphide particles under flotation-related conditions, *Colloids Surf. A* **106**, 203 (1996).
- [8] O. I. Vinogradova, G. E. Yakubov, and H.-J. Butt, Forces between polystyrene surfaces in water–electrolyte solutions: Long-range attraction of two types? *J. Chem. Phys.* **114**, 8124 (2001).
- [9] A. Tonck, J. M. Georges, and J. L. Loubet, Measurements of intermolecular forces and the rheology of dodecane between alumina surfaces, *J. Colloid Interface Sci.* **126**, 150 (1988).
- [10] E. J. W. Verwey and J. Th. G. Overbeek, Long distance forces acting between colloidal particles, *Trans. Faraday Soc.* **42**, B117 (1946).
- [11] B. Derjaguin and L. Landau, Theory of the stability of strongly charged lyophobic sols and of the adhesion of strongly charged particles in solutions of electrolytes, *Prog. Surf. Sci.* **43**, 30 (1993).
- [12] M. Valtiner and G. Grundmeier, Single molecules as sensors for local molecular adhesion studies, *Langmuir* **26**, 815 (2010).
- [13] F. Borghi, V. Vyas, A. Podestà, and P. Milani, Nanoscale roughness and morphology affect the IsoElectric point of titania surfaces, *PLoS One* **8**, e68655 (2013).
- [14] J. Duval, J. Lyklema, J. M. Kleijn, and H. P. van Leeuwen, Amphifunctionally electrified interfaces: Coupling of electronic and ionic surface-charging processes, *Langmuir* **17**, 7573 (2001).
- [15] V. B. Svetovoy and G. Palasantzas, Influence of surface roughness on dispersion forces, *Adv. Colloid Interface Sci.* **216**, 1 (2015).
- [16] P. J. van Zwol, G. Palasantzas, and J. Th. M. DeHosson, Weak dispersive forces between glass and gold macroscopic surfaces in alcohols, *Phys. Rev. E* **79**, 041605 (2009).
- [17] R. BakhshandehSeraji and G. Palasantzas, Nanoscale-roughness influence on pull-off adhesion force in liquid and air, *Phys. Rev. E* **108**, 054801 (2023).
- [18] J. N. Munday, F. Capasso, V. A. Parsegian, and S. M. Bezrukov, Measurements of the Casimir-Lifshitz force in fluids: The effect of electrostatic forces and Debye screening, *Phys. Rev. A* **78**, 032109 (2008).
- [19] P. J. van Zwol, V. B. Svetovoy, and G. Palasantzas, Distance upon contact: Determination from roughness profile, *Phys. Rev. B* **80**, 235401 (2009).
- [20] B. V. Derjaguin, N. V. Churaev, and V. M. Muller, *Surface Forces* (Springer, Boston, 1987).
- [21] See Supplemental Material at <http://link.aps.org/supplemental/10.1103/PhysRevB.110.035416> for IX.A We describe the numerical implementation of the Casimir force. IX.B We describe the numerical implementation of the nonlinear Poisson Boltzmann equation and analyze some of its consequences. IX.C We describe the numerical implementation of the maximum likelihood model and search. IX.D We present detailed numerical values for our fits. Including the values of sigma.
- [22] P. Bruno, Long-range magnetic interaction due to the Casimir effect, *Phys. Rev. Lett.* **88**, 240401 (2002).
- [23] V. B. Svetovoy, P. J. van Zwol, G. Palasantzas, and J. Th. M. De Hosson, Optical properties of gold films and the Casimir force, *Phys. Rev. B* **77**, 035439 (2008).
- [24] C.-C. Chang, A. A. Banishev, R. Castillo-Garza, G. L. Klimchitskaya, V. M. Mostepanenko, and U. Mohideen, Gradient of the Casimir force between Au surfaces of a sphere and a plate measured using an atomic force microscope in a frequency-shift technique, *Phys. Rev. B* **85**, 165443 (2012).
- [25] R. S. Decca, D. López, E. Fischbach, G. L. Klimchitskaya, D. E. Krause, and V. M. Mostepanenko, Tests of new physics from precise measurements of the Casimir pressure between two gold-coated plates, *Phys. Rev. D* **75**, 077101 (2007).
- [26] V. M. Mostepanenko and N. N. Trunov, The Casimir effect and its applications, *Sov. Phys. Usp.* **31**, 965 (1988).
- [27] C. J. Van Oss, M. K. Chaudhury, and R. J. Good, Interfacial Lifshitz-van der Waals and polar interactions in macroscopic systems, *Chem. Rev.* **88**, 927 (1988).
- [28] N. V. Churaev, B. V. Derjaguin, and V. M. Muller, *Surface Forces* (Springer Science & Business Media, New York, 2013).
- [29] A. Le Cunuder, A. Petrosyan, G. Palasantzas, V. Svetovoy, and S. Ciliberto, Measurement of the Casimir force in a gas and in a liquid, *Phys. Rev. B* **98**, 201408(R) (2018).
- [30] W. Broer, G. Palasantzas, J. Knoester, and V. B. Svetovoy, Roughness correction to the Casimir force beyond perturbation theory, *Europhys. Lett.* **95**, 30001 (2011).
- [31] J. A. Greenwood, J. B. P. Williamson, and F. P. Bowden, Contact of nominally flat surfaces, *Proc. R. Soc. London Ser. A* **295**, 300 (1966).
- [32] I. A. Soldatenkov, G. Palasantzas, and V. B. Svetovoy, Weak adhesion between deposited rough films: Relation to dispersion forces, *Phys. Rev. B* **104**, L121404 (2021).
- [33] J. Bloomenthal, Polygonization of implicit surfaces, *Comput. Aided Geom. Des.* **5**, 341 (1988).
- [34] P. A. Maia Neto, F. S. S. Rosa, L. B. Pires, A. B. Moraes, A. Canaguier-Durand, R. Guérout, A. Lambrecht, and S. Reynaud, Scattering theory of the screened Casimir interaction in electrolytes, *Eur. Phys. J. D* **73**, 178 (2019).